Mesh Simplification Based on Edge Collapsing Could Improve Computational Efficiency in Near Infrared Optical Tomographic Imaging

Dilip Mathew Thomas, Phaneendra K. Yalavarthy, Deepak Karkala, and Vijay Natarajan

Abstract—**The diffusion equation-based modeling of near infrared light propagation in tissue is achieved by using finite-element mesh for imaging real-tissue types, such as breast and brain. The finite-element mesh size (number of nodes) dictates the parameter space in the optical tomographic imaging. Most commonly used finite-element meshing algorithms do not provide the flexibility of distinct nodal spacing in different regions of imaging domain to take the sensitivity of the problem into consideration. This study aims to present a computationally efficient mesh simplification method that can be used as a preprocessing step to iterative image reconstruction, where the finite-element mesh is simplified by using an edge collapsing algorithm to reduce the parameter space at regions where the sensitivity of the problem is relatively low. It is shown, using simulations and experimental phantom data for simple meshes/domains, that a significant reduction in parameter space could be achieved without compromising on the reconstructed image quality. The maximum errors observed by using the simplified meshes were less than 0.27% in the forward problem and 5% for inverse problem.**

Index Terms—**Diffuse optical tomography, image reconstruction, mesh simplification, near infrared imaging, 3-D imaging.**

I. Introduction

Diffuse optical tomography has the potential to become an adjunct imaging modality for breast and brain imaging due to its capability to provide functional images using nonionizing near infrared (NIR) light as the interrogating media [1]–[3]. Typically the NIR light, wavelength in the range of 600–1000 nm, is delivered and collected using fiber bundles at the boundary of tissue. These boundary measurements are used to reconstruct the internal distributions of optical absorption and scattering coefficients. Reconstructed optical absorption and scattering coefficients at multiple wavelengths will lead to functional images of the tissue under investigation [3].

As the light propagation at these NIR wavelengths is dominated by scattering [4], the modeling of light propagation for thick tissue is performed using diffusion equation (DE) [5]. The partial differential equation (PDE) that describes the light propagation, i.e., DE, is solved using the finite-element method (FEM) due to its capability to handle complicated geometries, such as breast and brain [5]–[7]. The FEM relies on the discretization of domain into a grid, typically consisting of triangles or tetrahedra. The PDE to be solved is assembled over this discretized domain using the basis functions. The assembled linear system of equations will give a numerically stable solution for the complicated geometries. As near infrared optical tomography inverse problem (reconstruction procedure) relies on solving the PDE repeatedly, the finite-element discretization plays an important role in terms of modeling accuracy and the number of reconstruction parameters [6], [8]. The number of reconstruction parameters for single wavelength case is twice the discretization points (number of nodes/vertices) in the finite-element mesh, where the factor of two appears as both optical absorption and reduced scattering coefficients are unknown.

Most molecular imaging techniques that requires solving DE relies on the finite-element meshes, where resolution of the reconstructed image is dependent on the nodal spacing in the finite-element mesh. Also, it has been well known that the generation of 3-D meshes within a close range of desired nodal spacing is achievable using most of the commercial and open-source mesh generators [9], [10]. As 3-D imaging problems tend to be highly underdetermined [11], the choice of uniform nodal spacing results in higher computational complexity compared to meshes that have different nodal spacing for different regions depending on the sensitivity of the problem. There were attempts earlier to use adaptive meshing algorithms in DE-based tomographic image reconstruction procedure [12], where the emphasis was on refining a coarse mesh at the region of heterogenity. These adaptive meshing schemes have resulted in improving the qualitative/quantitative nature of reconstructed heterogeneities at an additional computational cost [12]. The main drawback of these adaptive meshing algorithms is that they are very sensitive to the changes in the imaging parameters and artifacts, typically happening at initial iterations, which leads to refinement in the undesired locations of the imaging volume [12], [13]. This leads to unnecessary computation. The earlier work by Eames

Manuscript received August 30, 2011; revised October 21, 2011 and December 30, 2011; accepted February 3, 2012. This work was supported by the Department of Atomic Energy Young Scientist Research Award (No. 2010/20/34/6/BRNS) by the Government of India. The work of V. Natarajan was supported by the Department of Science and Technology, Indian Institute of Science, India, under Grant SR/S3/EECE/048/2007 and SR/S4/MS:419/07.

D. M. Thomas is with the Department of Computer Science and Automation, Indian Institute of Science, Bangalore 560012, India (e-mail: dilip@csa.iisc.ernet.in).

P. K. Yalavarthy and D. Karkala are with the Supercomputer Education and Research Centre, Indian Institute of Science, Bangalore 560012, India (e-mail: phani@serc.iisc.ernet.in; deepak_karkala@yahoo.co.in).

V. Natarajan is with the Department of Computer Science and Automation, and Supercomputer Education and Research Centre, Indian Institute of Science, Bangalore 560012, India (e-mail: vijayn@csa.iisc.ernet.in).

Color versions of one or more of the figures in this paper are available online at http://ieeexplore.ieee.org.

Digital Object Identifier 10.1109/JSTQE.2012.2187276

et al. [14] used the Jacobian reduction method (for the direct Newton-type algorithms) to reduce the computational complexity of the reconstruction problem by ignoring the nodes that do not lie in the most sensitive region of the imaging domain. The resulting images were comparable to the original (using full Jacobian) images. This approach reduced the computational complexity in terms of number of operations, but still required to construct a large memory-intensive full Jacobian matrix. The construction of the Jacobian consumes approximately 75% of the computational time in any given iteration [15].

This study addresses the simplification of finite-element mesh based on the sensitivity profile of the imaging domain with an aim to reduce the computational complexity of both forward and inverse problems in diffuse optical tomography. It will be shown that the proposed method here does simplification of the existing mesh by collapsing the edges outside the region of interest and does not require any computationally demanding procedure. The simplification of mesh is performed as a preprocessing step to diffuse optical tomographic image reconstruction procedure. The results from simulations and experimental gelatin phantom cases using the simplified meshes were compared and contrasted with the results obtained using the original mesh in terms of quantitative accuracy.

II. METHODS

A. Diffuse Optical Tomographic Image Reconstruction

The image reconstruction procedure in diffuse optical tomography is performed using iterative least-squares methods, where the modeled data ($G(\mu)$ with μ representing the set of optical properties) are matched with the experimental data y [5], [16]. The least-squares problem is typically solved by the Levenberg–Marquardt minimization scheme, described in detail in [16].

The finite-element-based frequency-domain diffusion model for the calculation of $G(\mu)$ is described in [7] and [17], here it is only briefly reviewed. The frequency-domain DE is given by [17]

$$-\nabla.D(r)\nabla\Phi(r,\omega) + \left(\mu_a(r) + \frac{i\omega}{c}\right)\Phi(r,\omega) = q_o(r,\omega) \tag{1}$$

where $q_o(r,\omega)$ represents the isotropic light source and c represents the speed of light in tissue. $\Phi(r,\omega)$ is photon density (complex values) at position r for the light modulation frequency of ω ($=2\pi f$, with $f = 100$ MHz). The absorption coefficient is represented by $\mu_a(r)$ and the diffusion coefficient by $D(r)$, defined as

$$D(r) = \frac{1}{3[\mu_a(r) + \mu_s'(r)]} \tag{2}$$

with $\mu_s'(r)$ representing the reduced scattering coefficient. The refractive-index mismatch at the tissue boundary is modeled using the Robin (type-III) boundary condition [18]. The μ in this study represents $[D(r); \mu_a(r)]$.

As described earlier, the imaging domain is discretized into linear triangular elements (for 2-D) or linear tetrahedral elements (for 3-D) connected at *NN* vertex nodes. As light propagates in 3-D [19], the discussion here is for 3-D domains with discretization elements as tetrahedra. The computational (forward) model for solving the DE leads to the linear system of equations as [7], [17]

$$M\Phi = q \tag{3}$$

where M is known as the mass matrix with a dimension of *NN* × *NN* (symmetric matrix) and is a function of μ, i.e., $\Phi = M^{-1}q = F(\mu)$, with M assembled over all elements of the finite-element mesh. q represents the forcing, including the source term ($q_o(r,\omega)$) and the boundary condition [17]. Sampling of Φ at the measurement position results in the modeled data, i.e., $G(\mu) = S\{\Phi\} = S\{F(\mu)\}$, where S represents the sampling matrix (containing source/detector positions) and F is the forward model [16]. M is highly sparse (with a banded structure in case of bandwidth optimized FE meshes) and typically sparse matrix solvers are used to obtain Φ [4], [17], [20].

The important computational step in the iterative image reconstruction procedure is to obtain jacobian ($J = \partial G(\mu)/\partial\mu$), in turn $G(\mu)$, which gives the rate of change in the modeled data with respect to optical properties. This J is typically obtained using the adjoint formulation [17], which requires solving the forward problem twice, one for the regular source term and another for adjoint source. The Jacobian J is calculated at every iteration. The iterative procedure of obtaining the solution starts with an initial guess for the optical properties μ_0 typically obtained using the calibration procedure of experimental data y [21], [22].

The frequency-domain data in this procedure are given by $y = [\ln(A);\ \theta]$ under the Rytov approximation, where $\ln(A)$ is the natural logarithm of amplitude A and θ is the phase of the frequency domain signal, making J a real valued matrix (dimension of 2*NM* × 2*NN*), where the *NM* represents the number of measurements [5], [16].

The objective function of the Levenberg–Marquardt (LM) minimization is given as [23], [24]

$$\Omega = \|y - G(\mu)\|^2. \tag{4}$$

The update equation (for getting $\triangle\mu$) for the LM minimization becomes [16]

$$(J^T J + \lambda I)\Delta\mu = J^T\ (y - G(\mu)) \tag{5}$$

where λ is the regularization parameter, chosen empirically (starts at 10 multiplied by the maximum of the diagonal values of $J^T J$ and reduced by a factor of $10^{0.25}$ at every subsequent iteration) and I is the identity matrix. The procedure for calculation of J, $G(\mu)$, and subsequently $\triangle\mu$ is repeated until the relative difference in the objective function [Ω, (4)] does not improve by more than 2%. Please note that solving (5) to obtain $\triangle\mu$ is a computational procedure with the number of operations of order $O\big((2 * (2NN)^3)/(3)\big)$ [25], [26].

As it is evident from the procedure, the computational burden of solving Eq. (5) highly depends on number of nodes/vertices (*NN*) of the FEM mesh. The next two sections will describe the procedure of meshing and its simplification that is used in this study.

III. MESH GENERATION

The finite-element mesh generation that is used in NIR imaging has been discussed in [9] and [10], it is only briefly reviewed here. In experimental cases, the finite-element meshing requires the surface profile of the imaging domain, which is either obtained by other imaging modality or stereotactic cameras. Initially, a surface mesh is created using 2-D delaunay using the surface profile of the imaging domain, followed by 3-D delaunay to give linear tetrahedral mesh. This is achieved either using commercial software packages like Mimics [27] or open-source platforms such as NETGEN [28] and MIVA [29]. In either case, the input parameters for the generation of tetrahedral volumetric mesh is either nodal spacing or number of desired nodes. The generated volumetric meshes typically go through a postprocessing step that makes sure that tetrahedral volumes in these finite elements are not close to zero (above the tolerance of the machine). These volumetric meshes are tagged with appropriate optical properties that can be used in the diffusion-based models. Note that the computation time associated with volume mesh generation is dependent on the segmentation procedure involved and nodal distance. This could be largely subjective as well, as most segmentation algorithms require input at various stages from the user. Also, generation of meshes that have different nodal distance in different parts of imaging domain tends to be difficult task and also results in instability in meshing algorithms [9], [10]. So, most commonly used meshing packages do not give the flexibility to vary the nodal distance in different regions of the imaging domain. It is always desirable that nodal distance for the whole imaging domain is kept constant by the user.

IV. MESH SIMPLIFICATION

The computational cost of the iterative image reconstruction procedure can be significantly reduced by using a lower resolution approximation of the original mesh. The original mesh here refers to the mesh that has initial values (guess) of the optical properties for starting the iterative reconstruction procedure typically obtained using data-calibration procedure [21], [22]. Simplification is done by iteratively collapsing edges of the mesh to generate a simplified mesh having fewer number of nodes. We identify a region of interest (ROI) that is a part of the imaging domain that has more sensitivity for a given source/detector location. The edges that lie outside the ROI are used in the simplification process, with an aim that this reduction of nodes does not affect the quality of the reconstructed images (also shown later). The simplification scheme, guided by the Quadric Error Metric [30], is computationally efficient and produces good quality mesh elements after simplification [31]. The details of the method is described in [30] and [31] and is briefly reviewed here.

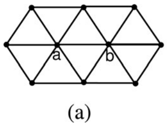

(a)

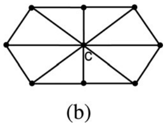

(b)

Fig. 1. (a) Edge ab is selected for collapse. (b) Edge ab is collapsed to c, the point that minimizes the sum of square distances to all hyperplanes.

In order to select edges for collapse in a manner that preserves the properties of the mesh, a cost is assigned to each edge of the mesh. Each node of the mesh has four coordinates, three of which are spatial coordinates and the fourth coordinate has value 0,1, or 2 to indicate the region to which the node belongs to (example: for breast mesh the regions could be fatty, fibroglandular, and tumor regions). Each node of the mesh is associated with a set of hyperplanes. Initially, the set of hyperplanes associated with a node corresponds to the tetrahedra incident on the node. These hyperplanes are used to determine the optimal coordinates for the new node created after an edge collapse. Each edge is collapsed to the point that minimizes the sum of square distances to the hyperplanes associated with the end points of the edge and this minimum distance is the cost assigned to the edge. The sum of squared distances from the new node to the hyperplanes is a measure of the local deviation from the input mesh together with the region labels. When an edge ab is collapsed to a new node c (refer to Fig. 1), the hyperplanes act as constraints and ensure the new node minimizes the error introduced by the edge collapse in representing the geometry of the boundary of the mesh as well as the region to which the node belongs and improves the quality of mesh elements.

Let H be a set of hyperplanes associated with a node and $v = (x, y, z, r)^T$ be any point in $\mathbb{R}^4$. Let $n_h = (x_h, y_h, z_h, r_h)^T$ be the unit normal to a hyperplane $h \in H$ and let p_h be a point in h. The squared distance D_h from v to h is given by the square of the magnitude of the projection of the vector $v - p_h$ onto n_h:

$$D_h = ((v - p_h)^T \cdot n_h)^2.$$

Let $d_h = -p_h^T \cdot n_h$. Then, D_h can be rewritten as

$$D_h = V^T (N_h \cdot N_h^T) V$$

where $V = (x, y, z, r, 1)^T$ and $N_h = (x_h, y_h, z_h, r_h, d_h)^T$. The sum of the squared distance from v to all hyperplanes in H is

$$D(v) = V^T \left(\sum_{h \in H} (N_h \cdot N_h^T) \right) V.$$

The 5 × 5 matrix $Q = \sum_{h \in H} (N_h \cdot N_h^T)$ is called as the fundamental quadric and is stored for each node. When an edge ab is collapsed to c, the fundamental quadric of c is computed as the sum of the fundamental quadrics of its end points (see Fig. 1). The location of c is determined by finding the value of v that minimizes $D(v)$. We round the fourth coordinate of v since the coordinate corresponding to region information can only take values 0, 1, or 2. The cost associated with each edge is this minimum sum of squared distance from c. We also use additional hyperplanes that act as constraints to preserve the geometry of the boundary of the mesh and to improve the quality of the mesh elements.

A. Choosing ROI

The ROI calculation is primarily based on the Jacobian of the forward problem, as it represents the sensitivity of the detected signal to a small change in the optical properties. As the Jacobian

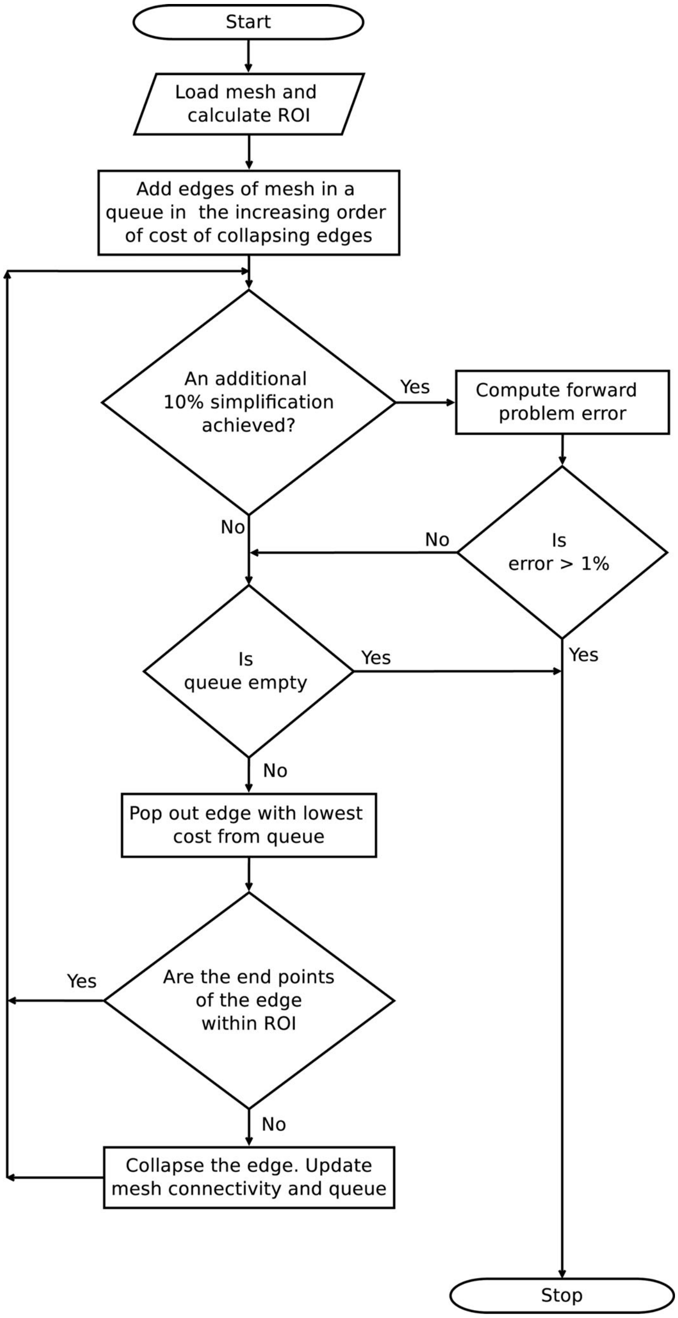

Fig. 2. Flowchart outlining major steps of the mesh simplification procedure based on edge collapsing.

has four kernels, the kernel that is chosen in determining the ROI is rate of change of logarithm of amplitude with respect to absorption coefficient. This Jacobian kernel, represented by $\bar{J}$, is summed over all the measurements (column sum) resulting in a 1-D vector (represented by $\hat{J}$, dimension of $NN \times 1$) that gives a relative numerical value for the sensitivity of each node. Mathematically

$$\hat{J}_j = \sum_{i=1}^{NM} \bar{J}_{ij} \text{ with } j = 1, 2, \ldots, NN. \tag{6}$$

Using the $\hat{J}$ nodes that are having less than 5% of the maximum sensitivity value are chosen to be used for the simplification (drawn from conclusions of [14]). The ROI contains the region that has atleast 5% or more relative sensitivity for given source/detector locations in the imaging domain. That is

$$\text{ROI} = \text{Region containing } j\text{'s with } \hat{J}_j \geq \frac{5}{100} * \max(\hat{J}). \tag{7}$$

Note that the ROI could be multiple regions depending on the source/detector configuration and imaging domain.

The flowchart in Fig. 2 shows the major steps involved in simplifying the given near infrared mesh. The initial cost of each edge is calculated and all edges are inserted into a priority queue. Candidate edges are selected for collapse outside the ROI in the order of increasing cost. During simplification, the end points of each candidate edge is checked to ensure that it lies outside the ROI. If yes, the edge is collapsed, otherwise it is rejected. This edge collapse (simplification) is continued iteratively by selecting edges from the priority queue till the queue becomes empty or the difference in $G(\mu)$ between the original and the simplified mesh exceeds 1%. The evaluation of $G(\mu)$ for the simplified mesh is not performed after each edge collapse, instead it is evaluated only at steps of 10% simplification, i.e., at 10%, 20%, and so on.

V. THREE-DIMENSIONAL MESHES

A. Numerical Experiments

In this study, meshes that are considered for simplification are derived from the volunteers/patients that have gone through the MRI–NIR studies at Dartmouth College. The volunteer identity numbers are designated for identifying the meshes. Along with these, cylindrical mesh and small-animal mouse mesh (mobi mesh) is used for completeness. The meshes have the nodes tagged with corresponding tissue types, for example, a breast mesh can have adipose, fibroglandular, and tumor. The mesh elements are linear tetrahedra. The background optical properties were $\mu_a = 0.01$ mm^{-1} and $\mu_s' = 1.0$ mm^{-1}. The region that is tagged as tumor had optical properties as $\mu_a = 0.02$ mm^{-1} and $\mu_s' = 2.0$ mm^{-1}. The refractive index of the imaging domain has been considered as 1.33. The data-collection geometry consisted of 16 fibers that were arranged in a circular, equally spaced fashion in the middle of the imaging domain. One fiber was used at a time as the source while other fibers were used as detectors to generate 240 (16×15) measurement locations or a total of 480 values (240 $\ln(A)$ data points and 240 θ data points). The sources were modeled as a Gaussian profile with a full-width half maximum of 3 mm to represent the distribution used in an experimental setup [32]. The source was also placed one mean transport scattering distance inside the boundary. To mimic the experimental case [32], a 1% noise in the amplitude and 1° in the phase has been added to the numerically generated data. The background optical properties were chosen as the initial guess for the iterative reconstruction procedure.

To effectively evaluate the algorithm, a cylindrical mesh that mimics the typical breast optical properties containing three regions (namely fatty, fibroglandular, and tumor) along with three-layers of data-collection is also considered. The data collection strategy is the same as the three-layers of in-plane data discussed in Section-II of [8]. This results in 720 measurement locations (3×240). The fatty and tumor optical properties are the same as the background and target optical properties discussed earlier. The fibroglandular region had optical properties, $\mu_a = 0.015$ mm^{-1} and $\mu_s' = 1.5$ mm^{-1}. The numerical experimental procedure that was followed was similar to the case of other meshes.

All computations were carried out on a Linux work station with an Intel Xeon 5410 Dual Quad Core 2.33 GHz processor with 64 GB of RAM.

B. Gelatin Phantom Experiment

A cylindrical gelatin phantom of diameter 86 mm, height 60 mm was fabricated using mixture of India ink for absorption and Titanium oxide (TiO_2) for scattering with a cylindrical hole extending in *Z*-direction (diameter 16 mm and height of 59 mm) placed close to the boundary. This gelatin phantom was fabricated by hardening heated gelatin solution consisting 80% deionized water and 20% gelatin (G2625, Sigma Inc.) along with different amounts of ink and TiO_2 (Sigma Inc) to result in background optical properties as $\mu_a = 0.008$ mm^{-1} and $\mu_s' = 0.9$ mm^{-1} at wavelength 785 nm using the phantom preparation procedure described in [33]. The background (gelatin) optical properties were estimated at the same wavelength on large cylindrical sample without the cylindrical hole using the procedure described in [21]. The cylindrical hole (mimicking the tumor) was filled with intralipid mixed with india ink to result in optical properties of $\mu_a = 0.02$ mm^{-1} and $\mu_s' = 1.0$ mm^{-1}, leading to have the contrast in only μ_a. The data were collected using only single layer of fibers (located in the middle of the phantom) resulting in 480 measurements. A cylindrical mesh consisting of 24161 nodes corresponding to 116757 linear tetrahedra elements was used as the original mesh (named as *phantom*) and the experimental data was calibrated using a reference homogeneous phantom data [21], [22]. Three-Dimensional volumetric rendering of optical properties showing the target distribution is given in the first column of Fig. 8.

VI. RESULTS

Using the mesh simplification methods discussed earlier, initially the identification of ROI was performed. After the ROI identification, the nodes that are lying outside the ROI were given as the input to the mesh simplification procedure (refer to Fig. 2). The simplification was performed in steps, i.e., 10%, 20%, 30%, 40%, and 50% of the original number of nodes. Please note that this simplification, i.e., to achieve the 10% less number of nodes compared to original, is performed in the region outside the ROI. One such example for the volunteer ID 1915 along with indication of ROI is given in Fig. 3. The total number of nodes for this particular mesh were 18723 and the total number of nodes for the simplified mesh were 16850, 14978, 13106, 11233, and 9361 corresponding to 10%, 20%, 30%, 40%, and 50% simplification.

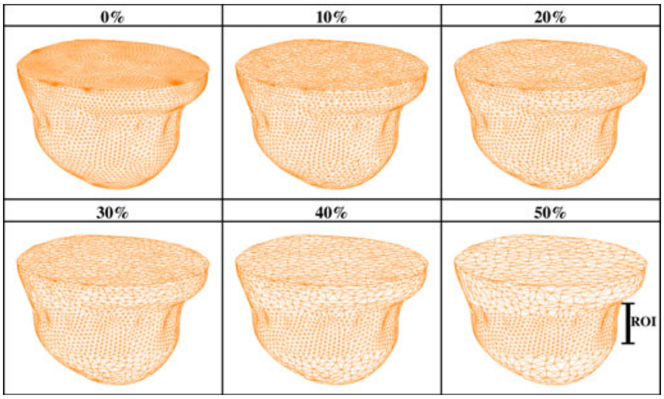

Fig. 3. Original and simplified finite-element meshes of a volunteer having patient ID as 1915. The simplified percentages are given on top of each mesh with 0% representing the original mesh. The computed ROI is shown in the 50% simplified mesh.

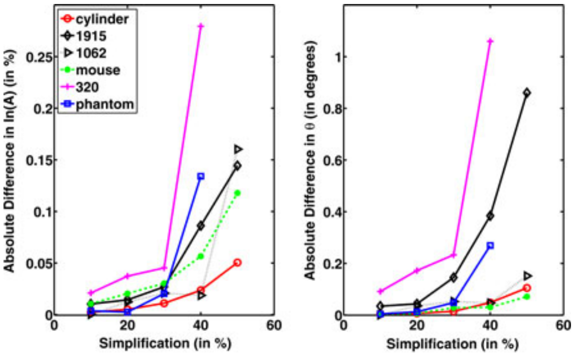

(a) (b)

Fig. 4. Plot of the forward problem error (with respect to the original mesh) versus simplification percentage in (a) ln(A) and (b) θ for different meshes considered in this study. The corresponding mesh ID/names are given in the legend of (a).

Next, the accuracy of the forward problem using the simplified meshes were assessed. Totally six meshes (including the phantom mesh) were considered for this study and the resulting plots giving the difference between original and simplified meshes (with simplification percentage given in the *x*-axis) is given in Fig. 4. The maximum error percentage for ln(A) is 0.27% and θ is 1.2° both for the patient mesh with ID as 320. It is also evident from Fig. 4 as the simplification increased (in turn reducing the total number of nodes) the error increased.

The reconstruction results (for one example case of 1915) using the simplified meshes given in Fig. 3 are given in Fig. 5 along with the target as the first column. Fig. 5(a) gives the reconstructed results using the standard reconstruction procedure. Fig. 5(b) represents the results obtained using hard priors [34], where the reconstruction parameter space is constrained to the number of regions segmented using other imaging modality (in here it is MRI). Qualitatively, by visual assessment, the reconstructed images using simplified meshes are similar to the ones obtained using the original mesh (with 0% simplification).

To assess the results observed in Fig. 5(a) quantitatively, the L_2-norm of the data model misfit with the iteration number is plotted and is shown in Fig. 6(a) for the simplified meshes

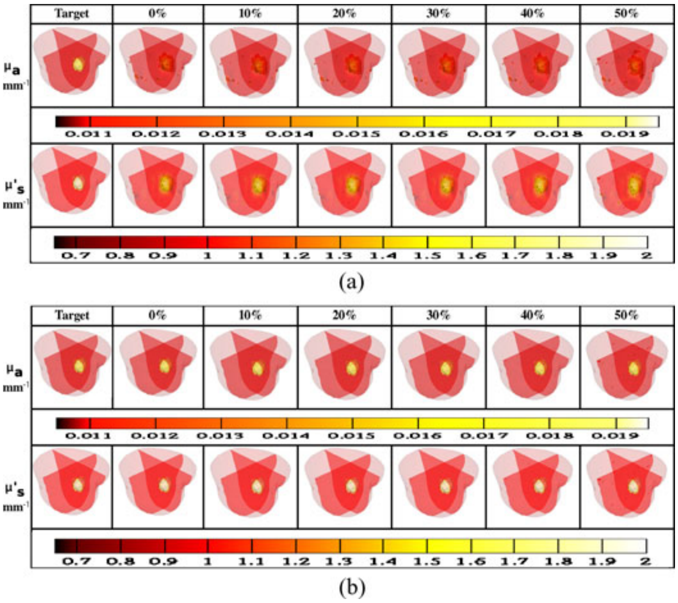

(a)

(b)

Fig. 5. Reconstructed distributions of μ_a and μ_s' using original and simplified meshes as given in Fig. 3 along with the target distributions (given in the first column) with (a). Standard image reconstruction algorithm with out any priors (b). Hard-prior-based reconstruction algorithm.

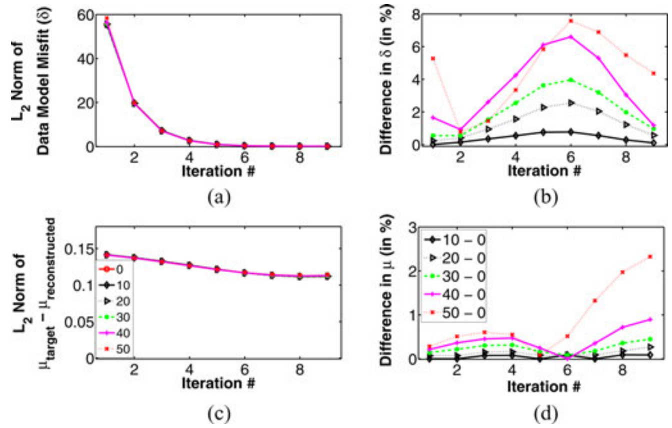

Fig. 6. Quantitative assessment of the data-model misfit and reconstruction parameter error versus the iteration number for results corresponding to Fig. 5(a). (a) L_2 norm of the data-model misfit for the original and simplified mesh (legend of (c) gives the simplification percentage with 0 corresponding to original mesh). (b) Difference (in %) between the simplified mesh and original mesh for results given in (a). The corresponding legend is given in (d). (c) L_2 norm of the difference between target and reconstructed optical parameters with varying simplification as given in the legend. (d) Difference (in %) between the simplified mesh and original mesh for results given in (c).

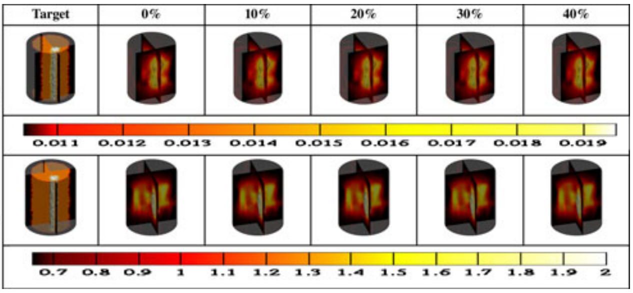

Fig. 7. Reconstructed distributions of μ_a and μ_s' using original and simplified meshes along with the target distributions (given in the first column) for a layered model that mimics typical breast and three layers of data collection with standard image reconstruction algorithm without any priors. The simplification percentage is given on the top of the figure (first row).

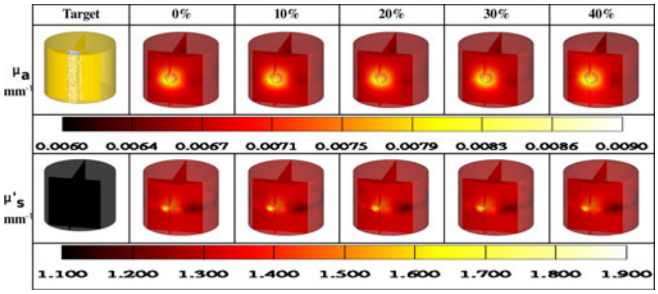

Fig. 8. Reconstructed distributions of μ_a and μ_s' using original and simplified meshes along with the target distributions (given in the first column) using experimental gelatin phantom data with standard image reconstruction algorithm without any priors. The simplification percentage is given on the top of the figure (first row).

along with ones obtained using original mesh [the simplification meshes are represented by percentage of simplification done given in the legend of Fig. 6(c)]. Similarly L_2-norm of the difference in the target and reconstructed optical properties are given in the Fig. 6(c). The difference plot [simplified – Original (0%)] corresponding to Fig. 6(a) and (c) is plotted in Fig. 6(b) and (d), respectively. The difference error is less than 8% and overall error percentage is less than 5% asserting that the reconstructed image quality has not been compromised using the simplified meshes. The same trend was observed for other meshes considered in this study, where the overall error percentage in the reconstructed parameters did not exceed more than 5%.

The reconstruction results using the standard reconstruction procedure for the cylindrical mesh that mimics the breast optical properties along with three layers of data collection are presented in Fig. 7. The maximum simplification percentage, where the forward problem errors are below 1% is only at 40%. Consistent with the results presented in Figs. 5(a) and 6, the difference in the forward and inverse problems in this case were less than 3%. The simplification of 50% was not achieved due to high forward problem error (around 10%), which was beyond the prescribed limit of 1%.

The experimental gelatin phantom reconstruction results using the standard reconstruction procedure that has contrast only in μ_a are given in Fig. 8. The fabricated gelatin phantom's height being only 60 mm, the achievable simplification is only upto 40% (beyond which the error in the forward problem was higher than 1%). Note that a boundary artifact in μ_s' was observed in this case. The achieved difference in the forward and inverse problems between original and simplified meshes for this experimental phantom case was less than 4%.

As the main discussion of this study is about reducing the computational complexity of the image reconstruction procedure, for meshes considered here, the total computational time taken for reconstruction for the simplified and original meshes are given in Table I including the number of iterations. The

TABLE I
TOTAL COMPUTATION TIME (IN SECONDS) FOR RECONSTRUCTION FOR DIFFERENT MESHES/DOMAINS USED IN THIS STUDY FOR VARYING SIMPLIFICATION PERCENTAGES INCLUDING THE NUMBER OF ITERATIONS (NO. IT)

Mesh	No. it	0%	10%	20%	30%	40%	50%	Over-head	Max R.F.
mouse	4	384.8	324	268.4	218.8	173.2	134	70.1	2.9
320	7	949.9	788.9	650.3	508.9	410.9	–	102.7	2.3
1062	13	5450.9	4266.6	3393	2421.9	1742	1196.9	310.2	4.6
1915	6	4327.8	3261.6	2488.2	1804.8	1282.8	888.6	543.4	4.9
Cylinder: 1layer	20	17522.2	13232.6	10154.9	7072.1	5016.3	3416.2	658.3	5.1
Cylinder: 3layers	15	20569.5	16417.5	12937.6	9889.5	7434	–	1023.3	2.8
Phantom	10	14029.1	10612.5	8301.3	5847.2	4068.1	–	1052.2	3.5

The last column gives the maximum reduction factor (max R.F.) in the computational time obtained by the mesh simplification. The column before that gives the overhead time for the simplification procedure.

overhead computational cost required for the simplification procedure is also given in the last column.

VII. DISCUSSION

Computational modeling of light propagation in complex domains, such as breast and brain, is a challenging problem. The finite-element approach to do the same is the most preferred technique due to its versatility in discretizing the imaging domain. As the computational model is used repeatedly in the iterative diffuse optical tomographic image reconstruction, any reduction in the computation time will immensely reduce the total computational complexity associated with this procedure. This study is aimed at achieving the same with finite-element mesh simplification, resulting in less number of imaging parameters.

As presented in the literature, 3-D meshing of complex imaging domain tends to be tedious and requires sufficient user input to get good quality meshes [9], [10]. Varying the nodal spacing for different parts of the imaging domain adds more complexity to the process and most commercial/open-source packages do not have this option. This study developed an easy and computationally efficient process, that uses edge collapsing, to result in a mesh that has varying nodal spacing depending on the sensitivity profile. This process was a precursor to the image reconstruction problem. The mesh simplification procedure is applied on a uniform mesh with optical properties typically obtained using data-calibration procedure [21], [22] and does not assume that target optical properties are known. The anatomical (structural priors) information of the imaging domain has no bearing on the simplification procedure, in case where structural priors are available, the algorithms preserve this information in the simplified meshes as well.

The simplified meshes were evaluated for forward and inverse problem accuracy, which has given error bounds to be less than 5%. For the forward problem it is less than 0.3% in amplitude and 1.2° in the phase (see Fig. 4). As the order of computation for each iteration of the image reconstruction procedure is $c(2NN)^3$, where *NN* is the number of nodes and c is a constant, reducing *NN* by 50% the computational complexity will be reduced by a factor of 8 (theoretically), which is now $c(NN)^3$. The overhead for the simplification procedure requires the calculation of Jacobian for calculation of ROI and running forward problem for every 10% simplification. The specific computational time associated with the cases discussed here are given in Table I. The maximum reduction factor in computational time that was achieved by the simplification procedure is 5.1 (cylinder: one layer case), which is lower than the theoretical estimate, primarily due to the fact that the computational cost is not only associated with number of operations, but also available memory for performing these operations. The overhead time was about 75% of time taken per iteration.

The meshes considered here were real 3-D breast meshes along with mouse and simple cylindrical meshes. The results showed similar trend for all of them, asserting that the methodology developed here is applicable for the complex and simple imaging domains, which have been discretized by using finite elements. Also, the choice of ROI is purely based on the sensitivity of the imaging domain, where no simplification is done, ensured that the error in the forward and inverse problem calculation are within the acceptable range. Also, the shape of the tumor using original and simplified meshes remained same (see Figs. 5, 7, and 8), resulting in identical results to prove that the developed methodology will not affect the over all image quality. As modern diffuse optical tomographic imaging systems typically collect data in 3-D (multilayer, specifically three layers), the same three layer data collection strategy with heterogeneous optical properties that mimics the breast optical properties were considered, in this case the ROI was atleast double in size compared to that of data collected using single layer. Even here, the simplification percentage that could be achieved is 40%. In this case, simplification beyond 40% and others over 50% lead to change in the boundary of the imaging volume, leading to inaccurate modeling of DE, where the forward problem errors were beyond 1%, leading to unmeaningful estimations of μ_a and μ_s' .

The experimental phantom case results (see Fig. 4 and 8) showed a promise of the developed methodology in improving the computational efficiency of image reconstruction procedure without compromising the quality of reconstructed images (see last column of Table I). Even though the reconstruction results showed a big artifact in μ_s' reconstruction at the boundary, the results were consistent between original and simplified procedure (see Fig. 8) ensuring that there is no bias in the reconstruction due to simplification even in the experimental data case. Note that simplification beyond 40% was unachievable as the the imaging domain consisted of large ROI due to height of the phantom being only 60 mm. The recovered contrast in μ_a in this experimental case is only about 40% of the expected as 3-D reconstruction is known to give poor performance in terms of contrast recovery [11]. Also, the cylindrical target was reconstructed in spherical shape as data was collected only using a single layer of fibers, leading to the sensitivity to fall very quickly beyond the layer of fibers [8].

It is important to note that in the cases considered here the ROI has turned out to be one single region extending in *Z*-direction leading to the simplification to be done in two separate parts of imaging domain, but the algorithm can simplify more than two parts, which might be needed when handling the complex data-collection systems/strategies that are currently being used [3].

The important step of ROI calculation is based on the initial guess of the optical properties, could be obtained using data-calibration procedure in the experimental cases [21], [22]. Typical data-calibration procedures, which assumes the imaging domain to be infinite/semi-infinite, involves removal of biases and/or numerical-model mismatch from the experimental data using analytical solution and results in obtaining the bulk optical properties of the tissue. As it uses the analytical models, the procedure is computationally inexpensive and results in optical properties close to the background values [21], [22], [35]. As the inverse problems are typically solved by the Newton-based framework [4], [5], [7], [16], it is essential that the initial guesses are close to the actual solution and any wrong guess can lead to erroneous results. The same can be expected in the case of simplified meshes.

The inverse problem in diffuse optical tomography could be solved using not only full-Newton (including Levenberg–Marquardt type) as discussed in this study, but with also gradient-based optimization techniques [3]. In the gradient-based techniques, even though there is no explicit calculation and storage of Jacobian, which tends to be memory intensive, there is a repeated usage of forward problem to calculate the gradient and to find the optimal step-size. As the mesh simplification procedure here reduces the parameter space significantly (upto 50%) in turn reducing the computational time in solving the forward problem, one can expect the discussion about reduction of computational complexity to be valid for these gradient-based optimization techniques as well.

Finite-element-based numerical models that solve DE are not limited to diffuse optical tomography, but are also used in tomographic imaging modalities that use bioluminescence [20] and fluorescence [36] as the contrast mechanism. Even though most results and discussion revolved around diffuse optical tomography, these imaging modalities can also get benefited by the developed methodology. As computational complexity in reconstructing tomographic optical images using a model-based iterative scheme is one of the main bottlenecks to get the imaging results in real time, methods of this type which reduce the computational burden become highly attractive to make optical imaging clinically viable.

VIII. CONCLUSION

The 3-D diffuse optical tomographic image reconstruction is a computationally intensive procedure due to the number of parameters that needs to be reconstructed. Most generic models use finite-element discretization for numerical modeling of DE, resulting in the number of parameters being a factor of number of nodes in the finite-element mesh. Meshing of 3-D volume with different nodal spacing for different regions is not possible using most of the commercial/open-source meshing environments, where the desirable mesh will have more nodes in the sensitive region (ROI) and lesser nodes else where. This study here aimed at introducing a methodology, where one can perform the mesh simplification procedure on a uniform nodal spaced mesh to achieve the same as a precursor to image reconstruction procedure. This mesh simplification procedure can reduce the computational complexity by a significant factor for 3-D imaging, without compromising on the reconstructed image quality. This procedure uses an edge collapsing algorithm that effectively reduces the number of nodes present in the mesh, thereby reducing the number of parameters. This methodology has been tested numerically and experimentally for realistic breast, mouse, and simple cylindrical meshes to assert that the computed image quality is comparable to the results obtained without simplification. The computational algorithms along with necessary instructions, are available on a web page [37] as an open source for the readers. Application of developed methodology for the patient cases with real data will be taken up as a future work.

ACKNOWLEDGMENT

The authors would like to thank the NIR imaging group at Dartmouth College for providing the necessary meshes and experimental data that were used in this study. They would also like to thank the anonymous reviewer for the constructive comments that improved the quality of this study.

REFERENCES

[1] D. A. Boas, D. H. Brooks, E. L. Miller, C. A. DiMarzio, M. Kilmer, R. J. Gaudette, and Q. Zhang, “Imaging the body with diffuse optical tomography,” *IEEE Signal Proc. Mag.*, vol. 18, no. 6, pp. 57–75, Nov. 2001.

[2] S. Srinivasan, B. W. Pogue, S. Jiang, H. Dehghani, C. Kogel, S. Soho, J. J. Gibson, T. D. Tosteson, S. P. Poplack, and K. D. Paulsen, “Interpreting hemoglobin and water concentration, oxygen saturation and scattering measured *in vivo* by near-infrared breast tomography,” *Proc. Nat. Acad. Sci. U.S.A.*, vol. 100, pp. 12349–12354, 2003.

[3] A. Gibson, J. C. Hebden, and S. R. Arridge, “Recent advances in diffuse optical tomography,” *Phys. Med. Biol.*, vol. 50, pp. R1–R43, 2005.

[4] S. R. Arridge and J. C. Hebden, “Optical imaging in medicine—II: Modelling and reconstruction,” *Phys. Med. Biol.*, vol. 42, pp. 841–853, 1997.

[5] S. R. Arridge, “Optical tomography in medical imaging,” *Inv. Prob.*, vol. 15, pp. R41–R93, 1999.

[6] M. Schweiger, S. R. Arridge, and D. T. Delpy, “Application of the finite element method for the forward and inverse models in optical tomography,” *J. Math. Imag. Vis.*, vol. 3, pp. 263–283, 1993.

[7] H. Dehghani, M. E. Eames, P. K. Yalavarthy, S. C. Davis, S. Srinivasan, C. M. Carpenter, B. W. Pogue, and K. D. Paulsen, “Near infrared optical tomography using NIRFAST: Algorithms for numerical model and image reconstruction algorithms,” *Commun. Numer. Meth. Eng.*, vol. 25, pp. 711–732, 2009.

[8] P. K. Yalavarthy, H. Dehghani, B. W. Pogue, and K. D. Paulsen, “Critical computational aspects of near infrared circular tomographic imaging: Analysis of measurement number, mesh resolution and reconstruction basis,” *Opt. Express*, vol. 14, pp. 6113–6127, 2006.

[9] S. Srinivasan, H. R. Ghadyani, B. W. Pogue, and K. D. Paulsen, “A coupled finite element-boundary element method for modeling Diffusion equation in 3D multi-modality optical imaging,” *Biomed. Opt. Express*, vol. 1, pp. 398–413, 2010.

[10] C. M. Carpenter, S. Srinivasan, B. W. Pogue, and K. D. Paulsen, "Methodology development for three-dimensional MR-guided near infrared spectroscopy of breast tumors," *Opt. Express*, vol. 16, pp. 17903–17914, 2008.
[11] P. K. Yalavarthy, D. R. Lynch, B. W. Pogue, H. Dehghani, and K. D. Paulsen, "Implementation of a computationally efficient least-squares algorithm for highly under-determined three-dimensional diffuse optical tomography problems," *Med. Phys.*, vol. 35, pp. 1682–1697, 2008.
[12] J. H. Lee, A. Joshi, and E. M. Sevick-Muraca, "Fully adaptive finite element based tomography using tetrahedral dual-meshing for fluorescence enhanced optical imaging in tissue," *Opt. Express*, vol. 15, pp. 6955–6975, 2007.
[13] L. Zhou, B. Yazõcõ, A. B. F. Ale, and V. Ntziachristos, "Performance evaluation of adaptive meshing algorithms for fluorescence diffuse optical tomography using experimental data," *Opt. Lett.*, vol. 35, pp. 3727–3729, 2010.
[14] M. Eames, B. W. Pogue, P. K. Yalavarthy, and H. Dehghani, "An efficient Jacobian reduction method for diffuse optical image reconstruction," *Opt. Express*, vol. 15, pp. 15908–15919, 2007.
[15] J. Prakash, V. Chandrasekharan, V. Upendra, and P. K. Yalavarthy, "Accelerating frequency-domain diffuse optical tomographic image reconstruction using graphics processing units," *J. Biomed. Opt.*, vol. 15, p. 066009, 2010.
[16] P. K. Yalavarthy, B. W. Pogue, H. Dehghani, and K. D. Paulsen, "Weight-matrix structured regularization provides optimal generalized least-squares estimate in diffuse optical tomography," *Med. Phys.*, vol. 34, no. 6, pp. 2085–2098, 2007.
[17] S. R. Arridge and M. Schweiger, "Photon-measurement density functions—Part 2: Finite-element-method calculations," *Appl. Opt.*, vol. 34, pp. 8026–8037, 1995.
[18] M. Schweiger, S. R. Arridge, M. Hiroaka, and D. T. Delpy, "The finite element model for the propagation of light in scattering media: Boundary and source conditions," *Med. Phys.*, vol. 22, pp. 1779–1792, 1995.
[19] M. Schweiger and S. R. Arridge, "Comparison of two- and three-dimensional reconstruction methods in optical tomography," *Appl. Opt.*, vol. 37, pp. 7419–7428, 1998.
[20] S. Ahn, A. J. Chaudhari, F. Darvas, C. A. Bouman, and R. M. Leahy, "Fast iterative image reconstruction methods for fully 3D multispectral bioluminescence tomography," *Phys. Med. Biol.*, vol. 53, pp. 3921–3942, 2008.
[21] B. W. Pogue, K. D. Paulsen, H. Kaufman, and C. Abele, "Calibration of near infrared frequency-domain tissue spectroscopy for absolute absorption coefcient quantitation in neonatal head-simulating phantoms," *J. Biomed. Opt.*, vol. 5, pp. 182–193, 2000.
[22] S. Jiang, B. W. Pogue, T. O. McBride, M. M. Doyley, S. P. Poplack, and K. D. Paulsen, "Near-infrared breast tomography calibration with opto-elastic tissue simulating phantoms," *J. Electron. Imag.*, vol. 12, pp. 613–620, 2003.
[23] K. Levenberg, "A method for the solution of certain nonlinear problems in least squares," *Q. Appl. Math.*, vol. 2, 164–168, 1944.
[24] D. W. Marquardt, "An algorithm for least squares estimation of nonlinear parameters," *J. Soc. Ind. Appl. Math.*, vol. 11, pp. 431–441, 1963.
[25] W. H. Press, S. A. Teukolsky, W. T. Vetterling, B. P. Flannery, *Numerical recipes: The art of Scientific Computing*, 3rd ed. New York: Cambridge Univ. Press, 2007.
[26] J. R. Westlake, *A Handbook of Numerical Matrix Inversion and Solution of Linear Equations*. New York: Wiley, 1968.
[27] [Online]. Available: http://www.materialise.com/mimics
[28] [Online]. Available: http://www.hpfem.jku.at/netgen/
[29] [Online]. Available: http://www.nitrc.org/projects/miva/
[30] M. Garland and P. S. Heckbert, "Surface simplification using quadric error metrics," *Comput. Graph.*, vol. 31, pp. 209–216, 1997.
[31] V. Natarajan and H. Edelsbrunner, "Simplification of three-dimensional density maps," *IEEE Trans. Vis. Comput. Graph.*, vol. 10, no. 5, pp. 587–597, Sep./Oct. 2004.
[32] T. O. Mcbride, B. W. Pogue, S. Jiang, U. L. Osterberg, and K. D. Paulsen, "A parallel-detection frequency-domain near-infrared tomography system for hemoglobin imaging of the breast *in vivo*," *Rev. Sci. Instr.*, vol. 72, pp. 1817–1824, 2001.
[33] B. W. Pogue and M. S. Patterson, "Review of tissue simulating phantoms for optical spectroscopy, imaging and dosimetry," *J. Biomed. Opt.*, vol. 11, p. 041102, 2006.
[34] P. K. Yalavarthy, B. W. Pogue, H. Dehghani, C. M. Carpenter, S. Jiang, and K. D. Paulsen, "Structural information within regularization matrices improves near infrared diffuse optical tomography," *Opt. Express*, vol. 15, pp. 8043–8058, 2007.
[35] E. M. C. Hillman, J. C. Hebden, F. E. W. Schmidt, S. R. Arridge, M. Schweiger, H. Dehghani, and D. T. Delpy, "Calibration techniques and datatype extraction for time-resolved optical tomography," *Rev. Sci. Instrum.*, vol. 71, pp. 3415–3427, 2000.
[36] S. C. Davis, H. Dehghani, J. Wang, S. Jiang, B. W. Pogue, and K. D. Paulse, "Image-guided diffuse optical fluorescence tomography implemented with Laplacian-type regularization," *Opt. Express*, vol. 15, pp. 4066–4082, 2007.
[37] [Online]. Available: http://www.serc.iisc.ernet.in/$\sim$phani/meshsim/

Dilip Mathew Thomas received the B.Tech. degree from the National Institute of Technology, Calicut, India, in 2002, and the M.E. degree from the Indian Institute of Science, Bengaluru, India, in 2009, both in computer science and engineering, where he is currently working toward the Ph.D. degree in computer science.

His research interests include scientific visualization and computational topology.

Phaneendra K. Yalavarthy received the M.Sc. degree in engineering from the Indian Institute of Science, Bangalore, India, in 2004, and the Ph.D. degree in biomedical computation from Dartmouth College, Hanover, NH, in 2007.

He is an Assistant Professor in the Supercomputer Education and Research Centre, Indian Institute of Science, Bangalore. His research interests include medical image computing, medical image analysis, and biomedical optics.

Deepak Karkala received the B.E. degree in electronics and communication engineering from the R.V. College of Engineering, Bangalore, India, in 2011.

He is currently a Junior Research Fellow in the Supercomputer Education and Research Centre, Indian Institute of Science, Bangalore, India. His research interests include medical image computing, three-dimensional medical imaging, and inverse problems in medical imaging.

Vijay Natarajan received the B.E. degree in computer science and the M.Sc. degree in mathematics from the Birla Institute of Technology and Science, Pilani, India, in 1999, and the Ph.D. degree in computer science from Duke University, Durham, NC, in 2004.

He is an Assistant Professor in the Department of Computer Science and Automation and Supercomputer Education and Research Centre, Indian Institute of Science, Bangalore, India. His research interests include scientific visualization, computational geometry, computational topology, and meshing.